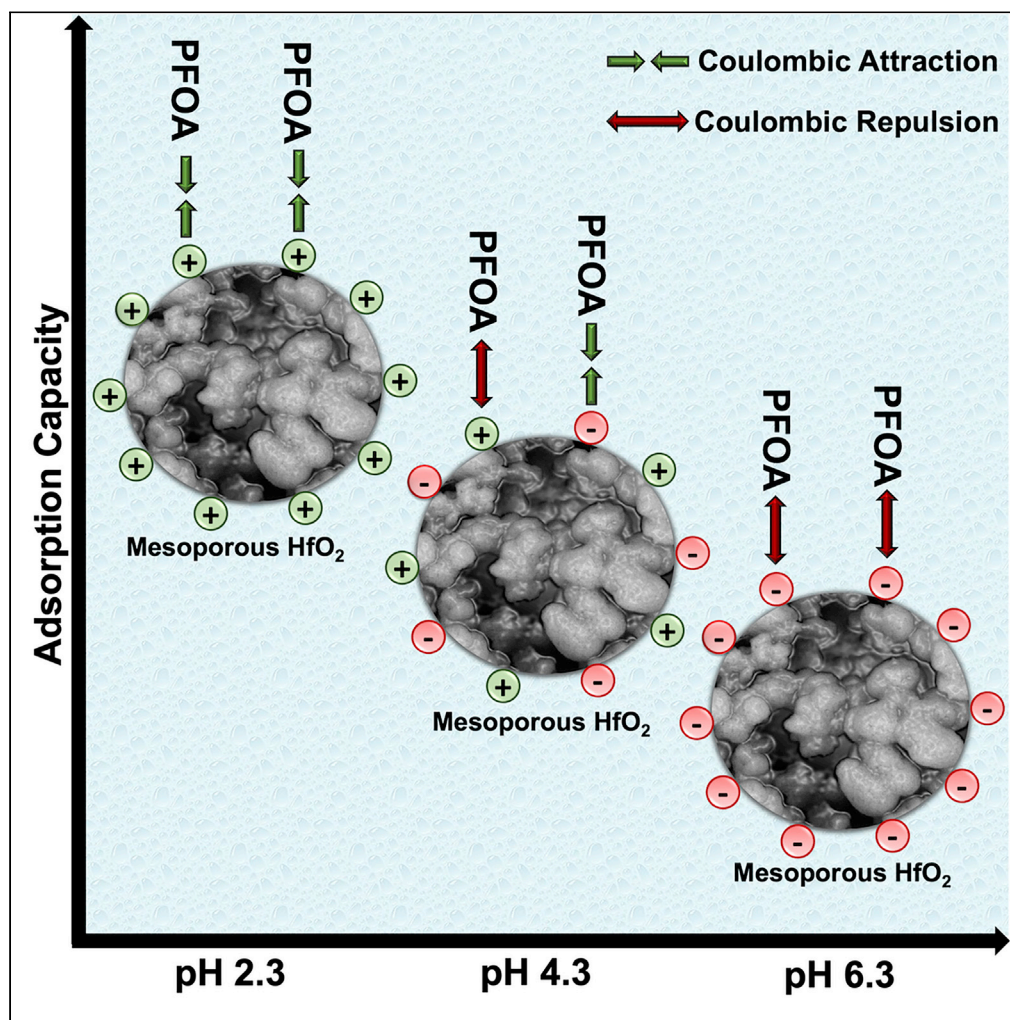# iScience

Article

Adsorption of perfluorooctanoic acid from water by pH-modulated Brönsted acid and base sites in mesoporous hafnium oxide ceramics

Fatima A. Hussain, Samuel E. Janisse, Marie C. Heffern, Maureen Kinyua, Jesús M. Velázquez

jevelazquez@ucdavis.edu

Highlights

The adsorption capacity of PFOA by MHO was determined to be 20.9 mg/g at pH 2.3

As pH increased, the adsorption capacity of MHO decreased due to Coulombic repulsions

MHO could be regenerated via calcination to limit the amount of toxic waste produced

Article

Adsorption of perfluorooctanoic acid from water by pH-modulated Brönsted acid and base sites in mesoporous hafnium oxide ceramics

Fatima A. Hussain,[1] Samuel E. Janisse,[1] Marie C. Heffern,[1] Maureen Kinyua,[2] and Jesús M. Velázquez[1,3,*]

SUMMARY

Per- and polyfluoroalkyl substances (PFAS) are increasingly appearing in drinking water sources globally. Our work focuses specifically on the adsorption of the legacy perfluorooctanoic acid (PFOA) using mesoporous hafnium oxide (MHO) ceramic synthesized via a sol-gel process. Experiments were performed at varying pH to determine the effect of surface charge on adsorption capacity of PFOA by MHO, and to postulate adsorption behavior. At pH 2.3, the adsorption capacity of PFOA on MHO was 20.9 mg/g, whereas at a higher pH of 6.3, it was much lower at 9.2 mg/g. This was due to increased coulombic attractions at lower pH between the positively charged conjugate acid active sites on MHO surface and negatively charged deprotonated PFOA anion in solution. After adsorption, the solid MHO was regenerated via calcination, reducing the amount of toxic solid waste to be disposed since the adsorbent is regenerated, and the PFOA is completely removed.

INTRODUCTION

Per- and polyfluoroalkyl substances (PFASs) are a group of over 4,000 industrial chemicals that have been widely synthesized for applications in water-proof clothing, carpets, cookware, and food packaging (Seltenrich, 2020; Sini et al., 2018; Sunderland et al., 2019; Zabaleta et al., 2017; Zheng and Salamova, 2020). They are used in food packaging and waterproof gear as they are thermally resistant, hydrophobic, and oleophobic (Glenn et al., 2021; Hill et al., 2017). The widespread industrial applicability of PFAS has led to large concentrations in already vulnerable aquatic environments (Lam et al., 2017). Perfluorooctanoic acid (PFOA), in particular, has become a serious cause for concern because it is environmentally persistent due to its high water solubility (9.5 g/L) and low volatility (Cordner et al., 2019; Seo et al., 2019; Sima and Jaffé, 2021; Zheng et al., 2012). PFOA does not bind well to soil or sediments, so it tends to persist in aquatic environments. In some cases, PFOA can present itself in drinking water leading to serious health effects (Post et al., 2012). PFAS in human bodies can target organs like the liver and kidney (Knutsen et al., 2018), and human bodily fluids like blood (Göckener et al., 2020; Guo et al., 2011) which can lead to thyroid disease (Coperchini et al., 2021), ulcerative colitis (Panikkar et al., 2019), reduced fertility (Velez et al., 2015), and several types of cancer depending on length of exposure (Bartell and Vieira, 2021; Shearer et al., 2021).

Developing techniques to remove PFOA from natural and drinking waters is of the essence. Various technologies exist to remove PFOA from water such as reverse osmosis (Patterson et al., 2019), electrochemical degradation using Yb-doped Ti/SnO_2–Sb/PbO_2 anodes (Ma et al., 2015), and photochemical decomposition by coexisting ferric ions and oxalic acids (Wang and Zhang, 2016). While reverse osmosis membranes are ideal due to their high removal capacity, modularity, and flexibility (Mastropietro et al., 2021), the process is non-destructive to PFAS creating secondary waste, and very energy-intensive (Coyle et al., 2021). Most membranes are very susceptible to fouling in extreme pH resulting in increased cost of treatment (Tang et al., 2007). Electrochemical degradation and photochemical decomposition of PFOA are destructive remediation techniques that decompose the PFOA molecule. However, decomposition leads to the generation of shorter chain PFAS, carbon dioxide, and fluoride ions which are still toxic and harmful to the environment (Liu et al., 2020; Trojanowicz et al., 2018). Consequently, economically feasible technologies that are functional in extreme chemical environments (e.g., extreme pH) are lacking to lower PFOA concentrations to safe levels.

[1]Department of Chemistry, University of California, One Shields Avenue, Davis, CA 95616, USA

[2]Department of Civil & Environmental Engineering, University of California, One Shields Avenue, Davis, CA 95616, USA

[3]Lead contact

*Correspondence: jevelazquez@ucdavis.edu
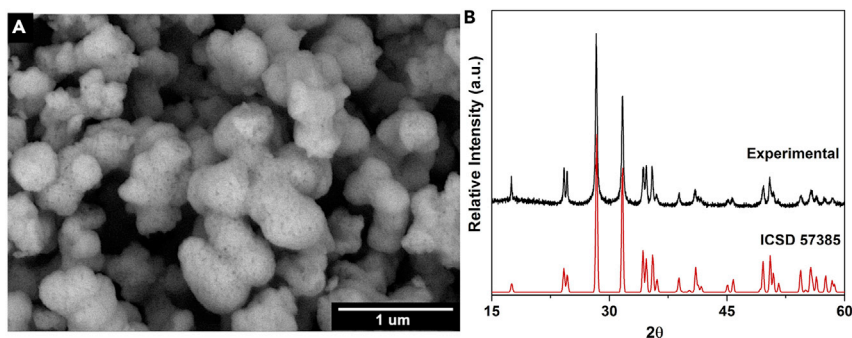
https://doi.org/10.1016/j.isci.2022.104138

Figure 1. Morphology and crystal structure of MHO ceramic
(A) ESEM image depicting particles of MHO with mesopores.
(B) XRD pattern with diffraction peaks for monoclinic MHO ceramic synthesized (top) overlaid with the published spectrum for monoclinic MHO ceramic (bottom, ICSD Collection Code 57385).

Alternatively, adsorption-based technologies are preferred due to their efficiency and economic benefits (Xu et al., 2020). Granular activated carbon (GAC) has been extensively studied due to its low cost and broad usability. However, the particle size of GAC (>100 μm) leads to relatively slow PFOA adsorption kinetics, which could also explain why the breakthrough point of PFOA in GAC is very fast (Yu et al., 2009). Regenerating GAC is also more complex as it requires heating at high temperatures (700°C–900°C) (Xiao et al., 2020) as well as chemical reactivation (Park et al., 2019). The high regeneration temperature may alter the physical and chemical properties of GAC, which in turn could affect the adsorption behavior (Siriwardena et al., 2021). Other adsorbents such as ion-exchange resins (Dixit et al., 2019), alumina (Wang and Shih, 2011), and quaternized cotton (Deng et al., 2012) are not thermally and chemically stable, which inhibits their regeneration efficacy (Alves et al., 2020). Mesoporous materials are beneficial for adsorption due to the ordered network of pores that can be tuned in size to trap contaminants, and chemically functionalized for selective adsorption (Zhao et al., 2012). There is a need for mesoporous adsorbents that have faster adsorption kinetics, are stable in harsh chemical conditions, and are thermally stable during regeneration.

Mesoporous hafnium oxide, a group IV transition metal oxide, is an attractive PFOA adsorption candidate. Mesoporous materials lead to increased PFOA adsorption as the diameter of PFOA is about 2 nm (Xiang et al., 2018), and previous work has shown that microporous materials (<2 nm) are not ideal for PFOA adsorption (Son et al., 2020). The high thermal (700°C) and chemical stability (active sites on the surface) of MHO ceramic, results from its highly coordinated hafnium. Hafnium can coordinate to seven oxygen atoms, whereas silicon, also in group IV, can only coordinate to four. Additionally, the chemical stability of hafnium oxide stems from the three tunable active sites: Lewis acid sites originating from unoccupied hafnium d orbitals, Brönsted acid sites, which donate a proton in basic media resulting in a negatively charged conjugate base active site, and Brönsted base sites which accept a proton in acidic media resulting in a positively charged conjugate acid active site (Figure S1) (Nawrocki et al., 1993). These active sites are stimulated at different pH conditions and may facilitate favorable interactions between the contaminant and the MHO ceramic surface.

The objective of this study is to investigate the kinetics and removal rate of PFOA from water using MHO ceramic under a range of pH conditions. MHO from sol-gel synthesis was used as the PFOA adsorbent. Adsorption experiments were performed over a period of 12 hours, which were then used to determine the maximum adsorption capacity of PFOA by MHO ceramic, the time needed to reach equilibrium, and construct adsorption isotherms. The concentrations of PFOA in liquid aliquots and solid MHO were measured using ^{19}F nuclear magnetic resonance spectroscopy and Fourier transform infrared spectroscopy, respectively.

RESULTS AND DISCUSSION

Morphology and crystal structure of MHO ceramic

The environmental scanning electron microscope (ESEM) image of the MHO ceramic powder is shown in Figure 1A. The particles in the image show very small black dots that represent the mesopores (2–50 nm) in
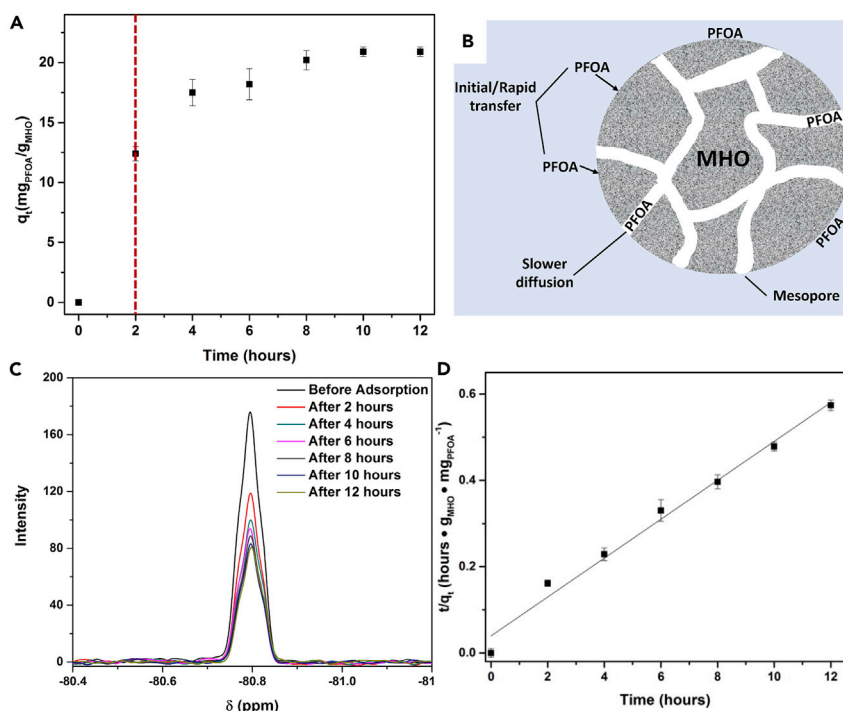
Figure 2. PFOA adsorption kinetics by MHO at 1,000 ppm

(A) Rate of PFOA adsorption on MHO at pH 2.3 using 1.25 g MHO ceramic, 50 mL of 1,000 ppm PFOA, over a period of 12 hours. Two-step adsorption process delineated using a red dotted line. Error bars represent standard deviation with n=3.

(B) Adsorption behavior of PFOA on MHO ceramic illustrating the rapid transfer of PFOA from solution to surface of MHO as well as slower diffusion of PFOA into the mesopores of MHO.

(C) Decrease in area of the terminal CF_3 peak in ^{19}F NMR of PFOA during adsorption on MHO.

(D) Pseudo-second-order model fit of the adsorption of PFOA on MHO. Error bars represent standard deviation with n=3.

the structure. The monoclinic crystal structure of the MHO ceramic was determined using X-ray diffraction (XRD) and compared to literature values as shown in Figure 1B. The results of the determination of the pH at the point of zero charge (pH_{PZC}) of MHO are shown in Figure S2. The pH_{PZC} was determined to be 4.7. The Brunauer-Emmet-Teller (BET) surface area of MHO was calculated using nitrogen gas adsorption isotherms to determine the porous surface area. The nitrogen adsorption isotherm is illustrated in Figure S3. The linear portion of the isotherm is used to determine BET surface area of MHO, which was 10.5 ± 0.6 m^2/g. The average pore size was determined using the Barrett-Joyner-Halenda (BJH) method to be 6.09 nm.

PFOA adsorption kinetics

Previous studies have indicated that PFOA adsorption on metal oxide surfaces is enhanced in acidic pH (Campos-Pereira et al., 2020). Therefore, the adsorption of PFOA on MHO was initially studied in an acidic pH of 2.3 to observe the rate of the reaction and kinetics of adsorption. Adsorption experiments over a 12 hour period (Figure 2A) show that the adsorption was very rapid in the first 2 hours, corresponding to the initial transfer of the PFOA onto the surface of MHO ceramic, followed by a relatively slower diffusion of the PFOA into the mesopores of MHO (Brusseau, 2020). Figure 2B illustrates this two-step adsorption behavior of PFOA onto the different MHO surface sites. Figure 2C shows the reduction of the integrated area of the terminal CF_3 peak in the ^{19}F nuclear magnetic resonance (NMR) signal; as expected, the largest change in area is observed in the first 2 hours of adsorption, followed by a visibly smaller decrease in the terminal CF_3 peak area. This is consistent with the two-step adsorption model for porous solid surfaces (Kennedy et al., 2007). A detailed ^{19}F NMR spectrum illustrating all the peaks corresponding to PFOA can be found in Figure S4. The MHO ceramic interface in water was easily accessible by PFOA, thus equilibrium was reached in 10 hours, and the MHO showed an adsorption capacity of 20.9 mg of PFOA/g of MHO. The rate of adsorption of PFOA on MHO ceramic from Figure 2A was fit with the pseudo-first-order model (Figure S5) and pseudo-second-order model (Figure 2D). The adsorption capacity at equilibrium

Table 1. Kinetic parameters of PFOA adsorption on MHO

Model	q_e (mg$_{PFOA}$/g$_{MHO}$)	Rate constant (k)	R^2
Pseudo-first-order	3.55 ± 0.08	0.147 ± 0.011 h^{-1}	0.965
Pseudo-second-order	22.2 ± 1.2	0.0513 ± 0.023 g$_{MHO}$/mg$_{PFOA}$ · hours	0.983

(q_e), rate constants (k), and R^2 values are reported for both models in Table 1. The reaction more closely follows the pseudo-second-order model.

The rate of adsorption of PFOA on MHO ceramic was compared to other state-of-the-art porous materials used for PFOA adsorption and summarized in Table S1. PFOA adsorption on MHO is very efficient in comparison to GAC (Yao et al., 2014) and boehmite (Wang et al., 2012) which required 24 and 48 hours to reach equilibrium, respectively. Boehmite (299.2 m^2/g) specifically had a much lower adsorption capacity at 1.89 mg/g; however, GAC (1,100 m^2/g) was more comparable at 22.7 mg/g. Commercially available multi-walled carbon nanotubes (350 m^2/g) had a shorter equilibrium time (4 hours) when compared to MHO; however, the adsorption capacity was also significantly lower at 12.4 mg/g (Yao et al., 2014). Silica (650 m^2/g), another group IV metal oxide, had an equilibrium time of 14 hours, and the adsorption capacity was 21.9 mg/g. However, the silica could not be regenerated after adsorption so it does limit its practicality (Stebel et al., 2019). IRA67 is an anion-exchange resin which adsorbs PFOA by ion exchange between the positively charged resin and the negatively charged head of PFOA and adsorption of the hydrophobic tail. In this case, the IRA67 resin had a higher adsorption capacity than MHO at 22.2 mg/g and a lower equilibrium time of 2 hours (Yao et al., 2014). However, methods to regenerate spent resins have not been fully developed to date. Despite MHO having a significantly lower BET surface area than all the ad-sorbents mentioned earlier, the adsorption capacity of PFOA is still comparable. That is due to the fact that mesoporous particles have larger external surface area and therefore more functional groups, such as Brönsted acid-base sites, that are available for PFOA adsorption (Kuvayskaya et al., 2020).

Results from adsorption experiments performed at a more environmentally relevant concentration of 1 ppm at pH 2.3 are illustrated in Figure 3 below. Similar to the adsorption experiments performed at an initial concentration of 1,000 ppm, the adsorption followed a two-step model where the initial adsorption of PFOA is rapid, corresponding to the initial transfer of PFOA from the solution onto the surface, followed by a relatively slower diffusion of PFOA into the mesopores (Figure 3A). The equilibrium time was 10 hours and the adsorption capacity was 24.3 ± 0.9 μg PFOA per gram of MHO due to the reduced initial concen-tration. The rate of adsorption of PFOA on MHO ceramic from Figure 3A was fit with the pseudo-first-order model (Figure S6) and pseudo-second-order model (Figure 3B). The adsorption capacity at equilibrium (q_e), rate constants (k), and R^2 values are reported for both models in Table S2. The reaction more closely follows the pseudo-second-order model. The two-step adsorption model for PFOA on MHO, as well as the pseudo-second-order nature of the adsorption process, was observed at both environmentally relevant starting concentration (1 ppm), and the higher concentration of 1,000 ppm.

PFOA adsorption isotherms

Experimental adsorption isotherms of PFOA on MHO ceramic were calculated with initial concentrations ranging from 200–1,000 ppm as shown in Figure 4. The adsorption isotherms were fitted by the Langmuir model and the Freundlich model using simple linear regression. Table S3 lists the isotherm constants ob-tained through the fitting. Based on the R^2 value, the Freundlich isotherm fit the data slightly better than the Langmuir isotherm. However, the Freundlich isotherm is not restricted to monolayer adsorption. The Freundlich model suggests that there are certain sites on the MHO that have an affinity for PFOA so the molecule will adsorb there first (Al-Ghouti and Da'ana, 2020).

pH-dependent adsorption of PFOA

pH is an important factor in adsorption experiments due to the strong reactivity of H$^+$ and OH$^-$ ions in so-lution (Wang and Shih, 2011). Previous work using silica has shown how various metal oxide active sites affect adsorption behavior of PFOA as a function of pH (Shafique et al., 2017). The effects of three different pH values (2.3, 4.3, and 6.3) on the adsorption of PFOA on MHO ceramic were tested, and the results are illustrated in Figure 5. These pH values were selected in order to study the effects of adsorption on MHO when the surface is positively charged (pH 2.3), neutral (pH 4.3), and negatively charged (pH 6.3). At pH 2.3,
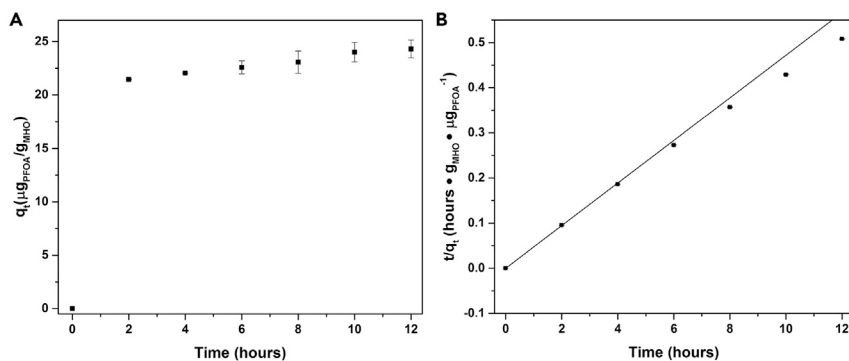
Figure 3. PFOA adsorption kinetics by MHO at 1 ppm

(A) Rate of PFOA adsorption on MHO at pH 2.3 using 1.25 g MHO ceramic, 50 mL of 1 ppm PFOA, over a period of 12 hours. Error bars represent standard deviation with n=3.

(B) Pseudo-second-order model fit of the adsorption of PFOA on MHO. Error bars represent standard deviation with n=3.

the adsorption capacity of PFOA on MHO was 20.9 ± 0.4 mg/g. The kinetics of adsorption of PFOA on MHO at pH 2.3 followed a clear two-step adsorption model as illustrated by the curve shape of the kinetic adsorption data in Figure 5. The first 2 hours were rapid adsorption on the surface followed by slow diffusion into the mesopores. As the pH increased, the adsorption capacity decreased to 13.0 ± 0.3 mg/g and 9.12 ± 0.5 mg/g at pH 4.3 and pH 6.3, respectively. The adsorption at pH 4.3 and 6.3 did not appear to follow a curved two-step adsorption model but rather a linear adsorption onto the surface. This is due to increased repulsion between PFOA anion and negatively charged conjugate base active site on MHO. The decrease in adsorption capacity of PFOA on MHO at various pH values is illustrated by the reduction of the ^{19}F NMR signal that corresponds to the terminal CF_3 peak as shown in Figure S7.

The driving forces behind the drastic change in adsorption capacity of PFOA on MHO as pH changes are illustrated in Figure 6. The pKa of PFOA is reported to be in the range of 0.5–3.8 (Burns et al., 2008), as shown in Figure 6B. At pH 2.3, the pH < point of zero charge (PZC) of MHO (4.7); therefore, the surface of the MHO is mostly positively charged with conjugate acid active sites. PFOA would be in equilibrium with the deprotonated PFOA anion at a pH of 2.3 since the pH is in the range of the pKa. This leads to coulombic attraction between the positively charged conjugate acid active site of MHO and the PFOA anion, as depicted by the green arrow in Figure 6A. There will also be some hydrophobic interaction
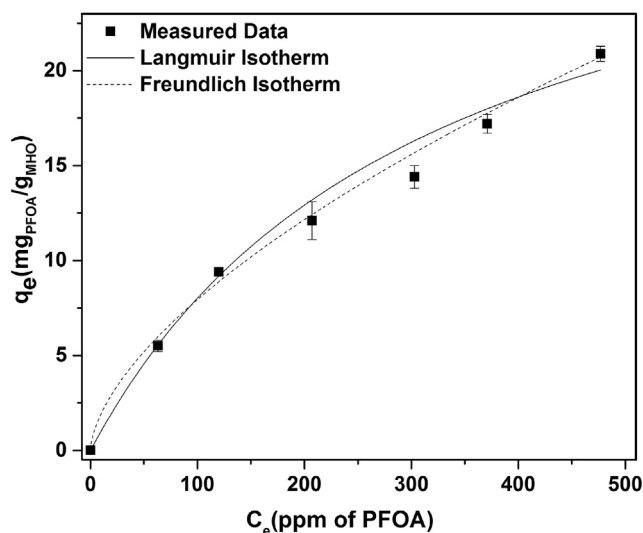

Figure 4. PFOA adsorption isotherms

Adsorption of PFOA on MHO ceramic fitted using the Langmuir isotherm and the Freundlich isotherm at a room temperature of 24°C. Error bars represent standard deviation with n=3.
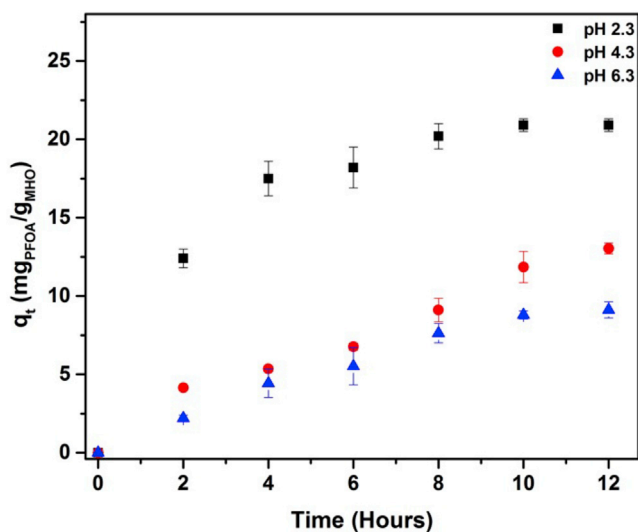
Figure 5. pH-dependent adsorption kinetics of PFOA
Rate of adsorption of PFOA on MHO at pH 2.3, 4.3, and 6.3. Error bars represent standard deviation with n=3.

between the hydrophobic tail of the PFOA molecule and the hydrophilic surface of MHO as depicted by the orange arrow in Figure 6A. At pH 4.3, the pH = PZC so the surface will be neutral, and the PFOA will exist mostly as the deprotonated anion since pH > pKa. Because there will be fewer positive conjugate acid active sites on the surface of MHO, there will be decreased coulombic attraction and some coulombic repulsion (Figure 6A, black arrow). Once the pH is at 6.3, the surface of the MHO is mostly negatively charged with conjugate base active sites since pH > PZC, and the PFOA will mostly exist as the deprotonated anion in solution. Both negatively charged species will lead to increased coulombic repulsion, and consequently decreased PFOA adsorption.

Analysis of MHO solid after adsorption of PFOA

Adsorption of PFOA on the solid MHO under different pH conditions was characterized using Fourier transform infrared (FTIR) spectroscopy. The resulting FTIR in Figure 7 reveals spectroscopic bands corresponding to PFOA, and shows that PFOA is adsorbed by the MHO ceramic. Figure 7A shows the spectrum between 1,450 and 1,800 cm^{-1}. The purple line represents pure solid PFOA, which is a perfluoro carboxylic acid that contains a carboxylate group (COOH) shown by the peak at 1,750 cm^{-1}. All the solid MHO samples after adsorption have a peak at 1,640 cm^{-1} which represents the deprotonated carboxylate group (COO-) (Chen et al., 2017). As the pH of adsorption increases, the intensity of the peak at 1,640 cm^{-1} increases. This corresponds to the fact that PFOA has a low pKa (3.8); therefore, as the pH increases the amount of COO- in solution also increases. This suggests that coulombic attractions between the PFOA anion and the positively charged conjugate acid active site on the MHO are the driving force of the adsorption. Figure 7B shows the spectrum from 950–1,450 cm^{-1} which is the range in which C-F bonds are typically observed. Peak 1 at 1,050 cm^{-1} denotes the C-C bond in the PFOA chain, peak 2 at 1,149 cm^{-1} represents the symmetric CF_2 stretch, peak 3 at 1,200 cm^{-1} represents the asymmetric stretching of CF_2 and CF_3, and peak 4 at 1,240 cm^{-1} is an asymmetric CF_2 stretch (Gao and Chorover, 2012). As the pH of adsorption increases, the intensity of the C-F peaks on MHO ceramic decreases. As the pH increases, there are fewer positively charged conjugate acid active sites on the surface of MHO, hence more repulsion between negatively charged conjugate base active site on MHO and PFOA anion. Because of the increased coulombic repulsion, it is harder for the PFOA to travel into the mesopores of MHO ceramic.

Regeneration of MHO ceramic after adsorption

The reusability of adsorbents used to remove PFOA is imperative for mitigating waste production, and reducing cleanup costs. Inadequate disposal techniques may lead to PFOA leaching back into the aquatic cycle. Thermal regeneration of PFOA-contaminated adsorbents may provide an opportunity to utilize
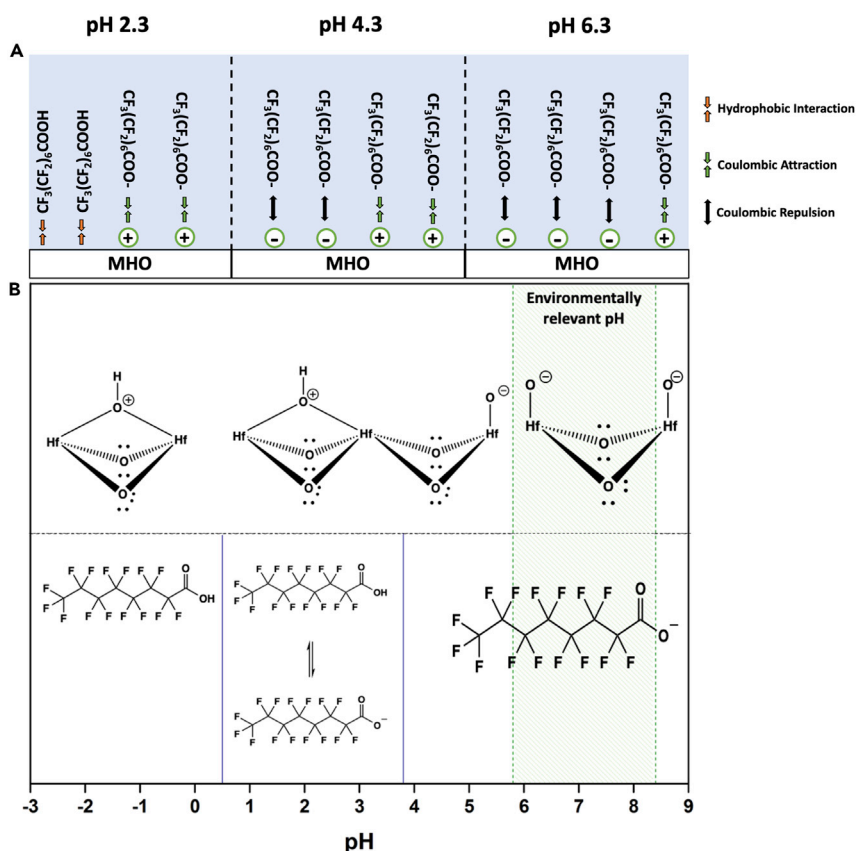
Figure 6. PFOA adsorption by pH-modulated Brönsted acid and base sites in MHO

(A) Illustration of PFOA adsorption on MHO at pH 2.3, 4.3, and 6.3.

(B) Description of MHO surface charge and PFOA charge as a function of pH. At pH < 4.7, MHO is positively charged with conjugate acid active sites, at pH 4.7, MHO has a neutrally charged surface, and at pH > 4.7, MHO is negatively charged with conjugate base active sites. pKa of PFOA is 0.5–3.8. At pH < pKa, the molecule does not dissociate in solution, at pH = pKa, the molecule is in equilibrium with the deprotonated anion, and at pH > pKa, the PFOA exists mostly as the deprotonated anion in solution.

existing regeneration framework to mineralize the adsorbed PFOA, and recover the spent adsorbent (Sonmez Baghirzade et al., 2021). Materials such as GAC (Watanabe et al., 2018) and multi-walled carbon nanotubes (Cao et al., 2018) have been regenerated by calcination. After adsorption, the MHO was calcined at 500°C for 20 minutes. This is relatively safer than using harsh and toxic chemicals to clean the material, as it does not produce excess toxic liquid waste. To compare the thermal stability and regeneration of MHO ceramic, thermogravimetric analysis (TGA) experiments were performed after PFOA adsorption. The MHO ceramic was heated to 750°C under high-purity argon flow. The results of the TGA are shown in Figure S8. The mass loss observed from heating the bare MHO ceramic before adsorption was very minimal at 0.16%, which is due to the evaporation of water from the hydrophilic surface. After PFOA adsorption, we see a mass loss of 1.01%, which corresponds to the PFOA evaporating from the MHO ceramic. To confirm this removal of PFOA from the MHO, the surface was analyzed using FTIR spectroscopy. The resulting spectrum is shown in Figure S9. The entire spectrum from 650 cm^{-1} to 4,000 cm^{-1} is shown in Figure S9A. It overlays the spectra of the PFOA standard, MHO before adsorption, MHO after adsorption in pH 2.3, and MHO after calcination. For MHO before adsorption, the peaks between 650–800 cm^{-1} correspond to monoclinic Hf-O and Hf-O_2. The low intensity peaks in the range of 1,200–1,600 cm^{-1} correspond to the carboxylate (COO-) ligand vibrations originating from the hydrolysis of N-methyl formamide during the sol-gel synthesis. The peak at 2,390 cm^{-1} represents the CO_2 that is alpha-coordinated to the Lewis acid sites on the surface (Hussain et al., 2020). The intensity of the COO- peak on the MHO after adsorption was clearly visible; however, the C-F peaks were very low in intensity, therefore Figure S9B shows the FTIR spectrum in the range of 950–1,800 cm^{-1} for clarity. From Figure S9B, the peaks from 1,000–1,400 cm^{-1} confirm the
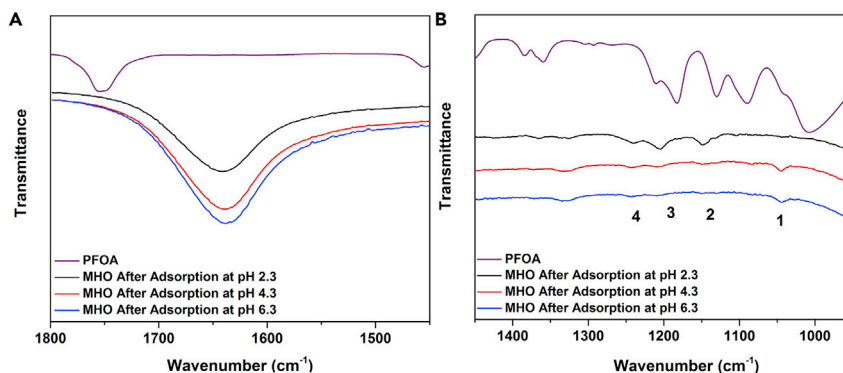
Figure 7. FTIR analysis of MHO solid after PFOA adsorption
FTIR of MHO ceramic after PFOA adsorption at pH 2.3, pH 4.3, and pH 6.3 in the range of (A) 1,450–1,800 cm^{-1} and (B) 950–1,450 cm^{-1}.

presence of PFOA on MHO after adsorption. After calcination, the surface of the MHO has no peaks corresponding to PFOA in the range of 950–1,800 cm^{-1}, which corresponds to the mass loss observed in TGA of MHO after adsorption. The MHO powders were also analyzed using XRD and ESEM after calcination to ensure that the crystal structure and morphology of the MHO also remained the same as before adsorption. The XRD shown in Figure S10 illustrates that the crystal structure remains monoclinic after heating. The ESEM in Figure S11 shows similar particles with mesopores as it did prior to calcination. The FTIR spectra of MHO after calcination confirm that PFOA was completely removed and that the MHO was regenerated.

The reusability of regenerated MHO was tested under three consecutive regeneration-adsorption cycles and the results are shown in Figure S12. After the first regeneration, the adsorption capacity of PFOA per gram of MHO at pH 2.3 was 19.96 ± 0.9 mg/g, which is slightly less than the as-synthesized MHO that has an adsorption capacity of 20.9 ± 0.4 mg/g at pH 2.3. After the second and third regeneration-adsorption cycles, the adsorption capacity of PFOA per gram of MHO was 19.85 ± 1 mg/g and 19.81 ± 0.6 mg/g, respectively. There is minimal loss in adsorption capacity of PFOA after regeneration of MHO; therefore, it shows promise for reusability.

Results from the desorption of PFOA from MHO surface showed that after 12 hours, the fraction of PFOA desorbed from the MHO surface accounted for 32% (±1) of the initial PFOA adsorbed. This desorption is due to the fact that during the initial stages of adsorption, the PFOA anion in solution is electrostatically attracted to the surface of MHO which makes the adsorption process rapid but also reversible since these coulombic forces are pH dependent. PFOA molecules have a hydrophilic functional group, and a hydrophobic tail, the latter of which facilitates hydrophobic interactions with the hydrophilic surface of MHO. These hydrophobic interactions are also weak physical forces that lead to weak binding of the contaminant to the surface. This hysteretic adsorption is common in multilayer physisorption using mesoporous materials (Yurdakal et al., 2019). Methods to address these issues with desorption, such as chemical functionalization of MHO, will be investigated in future work.

Conclusions

This work demonstrated the ability of MHO to adsorb PFOA from water despite its relatively low BET surface area. The adsorption capacity of PFOA on MHO was 20.9 ± 0.4 mg/g at pH 2.3 with an equilibrium time of 10 hours. As the pH increased, the adsorption capacity of MHO decreased. This is because increasing pH produces more negatively charged conjugate base active sites on the surface of MHO and more PFOA anion in solution. There will be coulombic repulsion between the adsorbent and the PFOA anion. However, at pH 2.3, the surface of MHO is positively charged with conjugate acid active sites so there will be coulombic attraction between the surface and the PFOA anion. The solid MHO could be easily regenerated after adsorption via calcination which reduces the amount of toxic solid waste that requires disposal after usage. The morphology, crystal structure, and surface functional groups remained the same before and after calcination.

Limitations of the study

The adsorption capacity of PFOA on MHO was low at environmentally relevant pH. Therefore, future studies would include developing methods to improve PFOA adsorption at environmentally relevant pH (5.8–8.4). This could be achieved by chemically functionalizing the surface with fluorophillic molecules such as 1H,1H,2H,2H-perfluorooctyltriethoxysilane (Kujawa et al., 2016) that binds to the active site on MHO, and consequentially increases the adsorption capacity even at environmentally relevant pH. Chemically functionalizing the surface could also lead to chemisorption of PFOA, which is a stronger interaction than physisorption of PFOA on the MHO surface. Moreover, chemisorption of PFOA molecules leads to reduced desorption of PFOA into solution (Zhang et al., 2021).

While thermal regeneration of adsorbents does not produce any excess toxic liquid waste, the PFOA does degrade to volatile PFAS molecules such as perfluoroheptene, C_2F_5, and C_2F_4. This is not a detoxification process, as the contaminants are released in gaseous form and contaminate the air (Xiao et al., 2020). Shorter chain PFAS molecules are more environmentally persistent, volatile, and spread easier, increasing the risk factor for infection (Li et al., 2020). Thermal regeneration is also a very energy-intensive process which is not economically feasible. Future studies will investigate less energy-intensive regeneration methods that do not produce any toxic waste, such as treating the spent adsorbents with ultra-violet (UV) radiation to photodegrade PFOA to fluoride ions (Li et al., 2020).

STAR★METHODS

Detailed methods are provided in the online version of this paper and include the following:

- KEY RESOURCES TABLE
- RESOURCE AVAILABILITY
  - ○ Lead contact
  - ○ Materials availability
  - ○ Data and code availability
- METHOD DETAILS
  - ○ Chemicals and materials
  - ○ MHO synthesis
  - ○ MHO characterization
  - ○ PFOA adsorption kinetics, isotherm models, and desorption
  - ○ MHO reusability for PFOA adsorption
  - ○ PFOA liquid analysis

SUPPLEMENTAL INFORMATION

Supplemental information can be found online at https://doi.org/10.1016/j.isci.2022.104138.

AUTHOR CONTRIBUTIONS

Fatima A Hussain: Conceptualization, Data curation, Formal analysis, Investigation, Methodology, Project administration, Validation, Visualization, Writing – original draft, Writing – review & editing. Samuel E. Janisse: Data Curation, Formal Analysis, Methodology, Visualization, Writing – review & editing. Marie C. Heffern: Resources, Supervision, Writing – review & editing. Maureen Kinyua: Supervision, Funding acquisition, Writing – original draft, Writing – review & editing. Jesús M. Velázquez: Conceptualization, Methodology, Resources, Supervision, Funding acquisition, Writing – original draft, Writing – review & editing.

REFERENCES

Al-Ghouti, M.A., and Da'ana, D.A. (2020). Guidelines for the use and interpretation of adsorption isotherm models: a review. J. Hazard. Mater. *393*, 122383. https://doi.org/10.1016/j.jhazmat.2020.122383.

Alves, A.V., Tsianou, M., and Alexandridis, P. (2020). Fluorinated surfactant adsorption on mineral surfaces: implications for PFAS fate and transport in the environment. Surfaces *3*, 516–566. https://doi.org/10.3390/surfaces3040037.

Bartell, S.M., and Vieira, V.M. (2021). Critical review on PFOA, kidney cancer, and testicular cancer. J. Air Waste Manage. Assoc. *71*, 663–679. https://doi.org/10.1080/10962247.2021.1909668.

Brinker, C.J., Sehgal, R., Hietala, S.L., Deshpande, R., Smith, D.M., Loy, D., and Ashley, C.S. (1994). Sol-gel strategies for controlled porosity inorganic materials. J. Memb. Sci. *94*, 85–102. https://doi.org/10.1016/0376-7388(93)E0129-8.

Brusseau, M.L. (2020). Simulating PFAS transport influenced by rate-limited multi-process retention. Water Res. *168*, 115179. https://doi.org/10.1016/j.watres.2019.115179.

Burns, D.C., Ellis, D.A., Li, H., McMurdo, C.J., and Webster, E. (2008). Experimental p K a determination for perfluorooctanoic acid (PFOA) and the potential impact of p K a concentration dependence on laboratory-measured partitioning phenomena and environmental modeling. Environ. Sci. Technol. *42*, 9283–9288. https://doi.org/10.1021/es802047v.

Campos-Pereira, H., Kleja, D.B., Sjöstedt, C., Ahrens, L., Klysubun, W., and Gustafsson, J.P. (2020). The adsorption of per- and polyfluoroalkyl substances (PFASs) onto ferrihydrite is governed by surface charge. Environ. Sci. Technol. *54*, 15722–15730. https://doi.org/10.1021/acs.est.0c01646.

Cao, F., Wang, L., Yao, Y., Wu, F., Sun, H., and Lu, S. (2018). Synthesis and application of a highly selective molecularly imprinted adsorbent based on multi-walled carbon nanotubes for selective removal of perfluorooctanoic acid. Environ. Sci. Water Res. Technol. *4*, 689–700. https://doi.org/10.1039/C7EW00443E.

Chen, W., Zhang, X., Mamadiev, M., and Wang, Z. (2017). Sorption of perfluorooctane sulfonate and perfluorooctanoate on polyacrylonitrile fiber-derived activated carbon fibers: in comparison with activated carbon. RSC Adv. *7*, 927–938. https://doi.org/10.1039/C6RA25230C.

Coperchini, F., Croce, L., Ricci, G., Magri, F., Rotondi, M., Imbriani, M., and Chiovato, L. (2021). Thyroid disrupting effects of old and new generation PFAS. Front. Endocrinol. (Lausanne) *11*. https://doi.org/10.3389/fendo.2020.612320.

Cordner, A., De La Rosa, V.Y., Schaider, L.A., Rudel, R.A., Richter, L., and Brown, P. (2019). Guideline levels for PFOA and PFOS in drinking water: the role of scientific uncertainty, risk assessment decisions, and social factors. J. Expo. Sci. Environ. Epidemiol. *29*, 157–171. https://doi.org/10.1038/s41370-018-0099-9.

Coyle, C., Ghosh, R., Leeson, A., and Thompson, T. (2021). US department of defense–funded Research on treatment of per- and polyfluoroalkyl substance–laden materials. Environ. Toxicol. Chem. *40*, 44–56. https://doi.org/10.1002/etc.4836.

Deng, S., Zheng, Y.Q., Xu, F.J., Wang, B., Huang, J., and Yu, G. (2012). Highly efficient sorption of perfluorooctane sulfonate and perfluorooctanoate on a quaternized cotton prepared by atom transfer radical polymerization. Chem. Eng. J. *193–194*, 154–160. https://doi.org/10.1016/j.cej.2012.04.005.

Dixit, F., Barbeau, B., Mostafavi, S.G., and Mohseni, M. (2019). PFOA and PFOS removal by ion exchange for water reuse and drinking applications: role of organic matter characteristics. Environ. Sci. Water Res. Technol. *5*, 1782–1795. https://doi.org/10.1039/C9EW00409B.

Gao, X., and Chorover, J. (2012). Adsorption of perfluorooctanoic acid and perfluorooctanesulfonic acid to iron oxide surfaces as studied by flow-through ATR-FTIR spectroscopy. Environ. Chem. *9*, 148. https://doi.org/10.1071/EN11119.

Glenn, G., Shogren, R., Jin, X., Orts, W., Hart-Cooper, W., and Olson, L. (2021). Per- and polyfluoroalkyl substances and their alternatives in paper food packaging. Compr. Rev. Food Sci. Food Saf. https://doi.org/10.1111/1541-4337.12726.

Göckener, B., Weber, T., Rüdel, H., Bücking, M., and Kolossa-Gehring, M. (2020). Human biomonitoring of per- and polyfluoroalkyl substances in German blood plasma samples from 1982 to 2019. Environ. Int. *145*, 106123. https://doi.org/10.1016/j.envint.2020.106123.

Guo, F., Zhong, Y., Wang, Y., Li, J., Zhang, J., Liu, J., Zhao, Y., and Wu, Y. (2011). Perfluorinated compounds in human blood around Bohai Sea, China. Chemosphere *85*, 156–162. https://doi.org/10.1016/j.chemosphere.2011.06.038.

Hill, P.J., Taylor, M., Goswami, P., and Blackburn, R.S. (2017). Substitution of PFAS chemistry in outdoor apparel and the impact on repellency performance. Chemosphere *181*, 500–507. https://doi.org/10.1016/j.chemosphere.2017.04.122.

Hussain, F.A., Zamora, J., Ferrer, I.M., Kinyua, M., and Velázquez, J.M. (2020). Adsorption of crude oil from crude oil–water emulsion by mesoporous hafnium oxide ceramics. Environ. Sci. Water Res. Technol. *6*, 2035–2042. https://doi.org/10.1039/D0EW00451K.

Kennedy, L.J., Vijaya, J.J., Kayalvizhi, K., and Sekaran, G. (2007). Adsorption of phenol from aqueous solutions using mesoporous carbon prepared by two-stage process. Chem. Eng. J. *132*, 279–287. https://doi.org/10.1016/j.cej.2007.01.009.

Knutsen, H.K., Alexander, J., Barregård, L., Bignami, M., Brüschweiler, B., Ceccatelli, S., Cottrill, B., Dinovi, M., Edler, L., Grasl-Kraupp, B., et al. (2018). Risk to human health related to the presence of perfluorooctane sulfonic acid and perfluorooctanoic acid in food. EFSA J. *16*, e05194. https://doi.org/10.2903/j.efsa.2018.5194.

Kujawa, J., Cerneaux, S., Kujawski, W., Bryjak, M., and Kujawski, J. (2016). How to functionalize ceramics by perfluoroalkylsilanes for membrane separation process? Properties and application of hydrophobized ceramic membranes. ACS Appl. Mater. Inter. *8*, 7564–7577. https://doi.org/10.1021/acsami.6b00140.

Kuvayskaya, A., Lotsi, B., Mohseni, R., and Vasiliev, A. (2020). Mesoporous adsorbents for perfluorinated compounds. Microporous Mesoporous Mater. *305*, 110374. https://doi.org/10.1016/j.micromeso.2020.110374.

Lam, N.H., Cho, C.-R., Kannan, K., and Cho, H.-S. (2017). A nationwide survey of perfluorinated alkyl substances in waters, sediment and biota collected from aquatic environment in Vietnam: distributions and bioconcentration profiles. J. Hazard. Mater. *323*, 116–127. https://doi.org/10.1016/j.jhazmat.2016.04.010.

Li, F., Wei, Z., He, K., Blaney, L., Cheng, X., Xu, T., Liu, W., and Zhao, D. (2020). A concentrate-and-destroy technique for degradation of perfluorooctanoic acid in water using a new adsorptive photocatalyst. Water Res. *185*, 116219. https://doi.org/10.1016/j.watres.2020.116219.

Liu, L., Liu, Y., Gao, B., Ji, R., Li, C., and Wang, S. (2020). Removal of perfluorooctanoic acid (PFOA) and perfluorooctane sulfonate (PFOS) from water by carbonaceous nanomaterials: a review. Crit. Rev. Environ. Sci. Technol. *50*, 2379–2414. https://doi.org/10.1080/10643389.2019.1700751.

Ma, Q., Liu, L., Cui, W., Li, R., Song, T., and Cui, Z. (2015). Electrochemical degradation of perfluorooctanoic acid (PFOA) by Yb-doped Ti/SnO 2 –Sb/PbO 2 anodes and determination of the optimal conditions. RSC Adv. *5*, 84856–84864. https://doi.org/10.1039/C5RA14299G.

Mastropietro, T.F., Bruno, R., Pardo, E., and Armentano, D. (2021). Reverse osmosis and nanofiltration membranes for highly efficient PFASs removal: overview, challenges and future perspectives. Dalt. Trans. *50*, 5398–5410. https://doi.org/10.1039/D1DT00360G.

Nawrocki, J., Rigney, M., McCormick, A., and Carr, P. (1993). Chemistry of zirconia and its use in chromatography. J. Chromatogr. A. *657*, 229–282.

Panikkar, B., Lemmond, B., Allen, L., DiPirro, C., and Kasper, S. (2019). Making the invisible visible: results of a community-led health survey following PFAS contamination of drinking water in Merrimack, New Hampshire. Environ. Heal. *18*, 79. https://doi.org/10.1186/s12940-019-0513-3.

Park, J.E., Lee, G.B., Hong, B.U., and Hwang, S.Y. (2019). Regeneration of activated carbons spent by waste water treatment using KOH chemical activation. Appl. Sci. *9*, 5132. https://doi.org/10.3390/app9235132.

Patterson, C., Burkhardt, J., Schupp, D., Krishnan, E.R., Dyment, S., Merritt, S., Zintek, L., and Kleinmaier, D. (2019). Effectiveness of point-of-use/point-of-entry systems to remove per- and polyfluoroalkyl substances from drinking water. AWWA Water Sci. *1*, e1131. https://doi.org/10.1002/aws2.1131.

Post, G.B., Cohn, P.D., and Cooper, K.R. (2012). Perfluorooctanoic acid (PFOA), an emerging drinking water contaminant: a critical review of recent literature. Environ. Res. *116*, 93–117. https://doi.org/10.1016/j.envres.2012.03.007.

Seltenrich, N. (2020). PFAS in food packaging: a hot, greasy exposure. Environ. Health Perspect. *128*, 054002. https://doi.org/10.1289/EHP6335.

Seo, S.-H., Son, M.-H., Shin, E.-S., Choi, S.-D., and Chang, Y.-S. (2019). Matrix-specific distribution and compositional profiles of perfluoroalkyl substances (PFASs) in multimedia environments. J. Hazard. Mater. *364*, 19–27. https://doi.org/10.1016/j.jhazmat.2018.10.012.

Shafique, U., Dorn, V., Paschke, A., and Schüürmann, G. (2017). Adsorption of perfluorocarboxylic acids at the silica surface. Chem. Commun. *53*, 589–592. https://doi.org/10.1039/C6CC07525H.

Shearer, J.J., Callahan, C.L., Calafat, A.M., Huang, W.-Y., Jones, R.R., Sabbisetti, V.S., Freedman, N.D., Sampson, J.N., Silverman, D.T., Purdue, M.P., and Hofmann, J.N. (2021). Serum concentrations of per- and polyfluoroalkyl substances and risk of renal cell carcinoma. JNCI J. Natl. Cancer Inst. *113*, 580–587. https://doi.org/10.1093/jnci/djaa143.

Sima, M.W., and Jaffé, P.R. (2021). A critical review of modeling Poly- and Perfluoroalkyl Substances (PFAS) in the soil-water environment. Sci. Total Environ. *757*, 143793. https://doi.org/10.1016/j.scitotenv.2020.143793.

Sini, K., Bourgeois, D., Idouhar, M., Carboni, M., and Meyer, D. (2018). Metal–organic framework sorbents for the removal of perfluorinated compounds in an aqueous environment. New J. Chem. *42*, 17889–17894. https://doi.org/10.1039/C8NJ03312A.

Siriwardena, D.P., James, R., Dasu, K., Thorn, J., Iery, R.D., Pala, F., Schumitz, D., Eastwood, S., and Burkitt, N. (2021). Regeneration of per- and polyfluoroalkyl substance-laden granular activated carbon using a solvent based technology. J. Environ. Manage. *289*, 112439. https://doi.org/10.1016/j.jenvman.2021.112439.

Son, H., Kim, T., Yoom, H.-S., Zhao, D., and An, B. (2020). The adsorption selectivity of short and long per- and polyfluoroalkyl substances (PFASs) from surface water using powder-activated carbon. Water *12*, 3287. https://doi.org/10.3390/w12113287.

Sonmez Baghirzade, B., Zhang, Y., Reuther, J.F., Saleh, N.B., Venkatesan, A.K., and Apul, O.G. (2021). Thermal regeneration of spent granular activated carbon presents an opportunity to break the forever PFAS cycle. Environ. Sci. Technol. *55*, 5608–5619. https://doi.org/10.1021/acs.est.0c08224.

Stebel, E.K., Pike, K.A., Nguyen, H., Hartmann, H.A., Klonowski, M.J., Lawrence, M.G., Collins, R.M., Hefner, C.E., and Edmiston, P.L. (2019). Absorption of short-chain to long-chain perfluoroalkyl substances using swellable organically modified silica. Environ. Sci. Water Res. Technol. *5*, 1854–1866. https://doi.org/10.1039/C9EW00364A.

Sunderland, E.M., Hu, X.C., Dassuncao, C., Tokranov, A.K., Wagner, C.C., and Allen, J.G. (2019). A review of the pathways of human exposure to poly- and perfluoroalkyl substances (PFASs) and present understanding of health effects. J. Expo. Sci. Environ. Epidemiol. *29*, 131–147. https://doi.org/10.1038/s41370-018-0094-1.

Tang, C.Y., Fu, Q.S., Criddle, C.S., and Leckie, J.O. (2007). Effect of flux (transmembrane pressure) and membrane properties on fouling and rejection of reverse osmosis and nanofiltration membranes treating perfluorooctane sulfonate containing wastewater. Environ. Sci. Technol. *41*, 2008–2014. https://doi.org/10.1021/es062052f.

Trojanowicz, M., Bojanowska-Czajka, A., Bartosiewicz, I., and Kulisa, K. (2018). Advanced Oxidation/Reduction Processes treatment for aqueous perfluorooctanoate (PFOA) and perfluorooctanesulfonate (PFOS) – a review of recent advances. Chem. Eng. J. *336*, 170–199. https://doi.org/10.1016/j.cej.2017.10.153.

Velez, M.P., Arbuckle, T.E., and Fraser, W.D. (2015). Maternal exposure to perfluorinated chemicals and reduced fecundity: the MIREC study. Hum. Reprod. *30*, 701–709. https://doi.org/10.1093/humrep/deu350.

Wang, F., Liu, C., and Shih, K. (2012). Adsorption behavior of perfluorooctanesulfonate (PFOS) and perfluorooctanoate (PFOA) on boehmite. Chemosphere *89*, 1009–1014. https://doi.org/10.1016/j.chemosphere.2012.06.071.

Wang, F., and Shih, K. (2011). Adsorption of perfluorooctanesulfonate (PFOS) and perfluorooctanoate (PFOA) on alumina: influence of solution pH and cations. Water Res. *45*, 2925–2930. https://doi.org/10.1016/j.watres.2011.03.007.

Wang, Y., and Zhang, P. (2016). Enhanced photochemical decomposition of environmentally persistent perfluorooctanoate by coexisting ferric ion and oxalate. Environ. Sci. Pollut. Res. *23*, 9660–9668. https://doi.org/10.1007/s11356-016-6205-4.

Watanabe, N., Takata, M., Takemine, S., and Yamamoto, K. (2018). Thermal mineralization behavior of PFOA, PFHxA, and PFOS during reactivation of granular activated carbon (GAC) in nitrogen atmosphere. Environ. Sci. Pollut. Res. *25*, 7200–7205. https://doi.org/10.1007/s11356-015-5353-2.

Xiang, L., Xiao, T., Yu, P.-F., Zhao, H.-M., Mo, C.-H., Li, Y.-W., Li, H., Cai, Q.-Y., Zhou, D.-M., and Wong, M.-H. (2018). Mechanism and implication of the sorption of perfluorooctanoic acid by varying soil size fractions. J. Agric. Food Chem. *66*, 11569–11579. https://doi.org/10.1021/acs.jafc.8b03492.

Xiao, F., Sasi, P.C., Yao, B., Kubátová, A., Golovko, S.A., Golovko, M.Y., and Soli, D. (2020). Thermal stability and decomposition of perfluoroalkyl substances on spent granular activated carbon. Environ. Sci. Technol. Lett. *7*, 343–350. https://doi.org/10.1021/acs.estlett.0c00114.

Xie, A., Dai, J., Chen, X., He, J., Chang, Z., Yan, Y., and Li, C. (2016). Hierarchical porous carbon materials derived from a waste paper towel with ultrafast and ultrahigh performance for adsorption of tetracycline. RSC Adv. *6*, 72985–72998. https://doi.org/10.1039/C6RA17286E.

Xu, J., Liu, Z., Zhao, D., Gao, N., and Fu, X. (2020). Enhanced adsorption of perfluorooctanoic acid (PFOA) from water by granular activated carbon supported magnetite nanoparticles. Sci. Total Environ. *723*, 137757. https://doi.org/10.1016/j.scitotenv.2020.137757.

Yao, Y., Volchek, K., Brown, C.E., Robinson, A., and Obal, T. (2014). Comparative study on adsorption of perfluorooctane sulfonate (PFOS) and perfluorooctanoate (PFOA) by different adsorbents in water. Water Sci. Technol. *70*, 1983–1991. https://doi.org/10.2166/wst.2014.445.

Yu, Q., Zhang, R., Deng, S., Huang, J., and Yu, G. (2009). Sorption of perfluorooctane sulfonate and perfluorooctanoate on activated carbons and resin: kinetic and isotherm study. Water Res. *43*, 1150–1158. https://doi.org/10.1016/j.watres.2008.12.001.

Yurdakal, S., Garlisi, C., Özcan, L., Bellardita, M., and Palmisano, G. (2019). (Photo)catalyst characterization techniques. In Heterogeneous Photocatalysis (Elsevier), pp. 87–152. https://doi.org/10.1016/B978-0-444-64015-4.00004-3.

Zabaleta, I., Negreira, N., Bizkarguenaga, E., Prieto, A., Covaci, A., and Zuloaga, O. (2017).

Screening and identification of per- and polyfluoroalkyl substances in microwave popcorn bags. Food Chem. *230*, 497–506. https://doi.org/10.1016/j.foodchem.2017.03.074.

Zhang, Z., Sarkar, D., Datta, R., and Deng, Y. (2021). Adsorption of perfluorooctanoic acid (PFOA) and perfluorooctanesulfonic acid (PFOS) by aluminum-based drinking water treatment residuals. J. Hazard. Mater. Lett. *2*, 100034. https://doi.org/10.1016/j.hazl.2021.100034.

Zhao, L., Qin, H., Wu, R., and Zou, H. (2012). Recent advances of mesoporous materials in sample preparation. J. Chromatogr. A. *1228*,

193–204. https://doi.org/10.1016/j.chroma.2011.09.051.

Zheng, G., and Salamova, A. (2020). Are melamine and its derivatives the alternatives for per- and polyfluoroalkyl substance (PFAS) fabric treatments in infant clothes? Environ. Sci. Technol. *54*, 10207–10216. https://doi.org/10.1021/acs.est.0c03035.

Zheng, X.-M., Liu, H.-L., Shi, W., Wei, S., Giesy, J.P., and Yu, H.-X. (2012). Effects of perfluorinated compounds on development of zebrafish embryos. Environ. Sci. Pollut. Res. *19*, 2498–2505. https://doi.org/10.1007/s11356-012-0977-y.

STAR★METHODS

KEY RESOURCES TABLE

REAGENT or RESOURCE	SOURCE	IDENTIFIER
Chemicals, peptides, and recombinant proteins		
Perfluorooctanoic acid	TCI America	CAS: 335-67-1
Deuterium oxide	Sigma-Aldrich	CAS: 7789-20-0
Trifluoroacetic acid	Acros Organics	CAS: 76-05-1
Sodium Chloride	Sigma-Aldrich	CAS: 7647-14-5
Sodium Hydroxide	Alfa Aesar	CAS: 1310-73-2
Sulfuric Acid	Sigma-Aldrich	CAS: 7664-93-9
Hydrochloric Acid	Sigma-Aldrich	CAS: 7647-01-0
Hafnium (IV) tetrachloride	Sigma-Aldrich	CAS: 13499-05-3
N-Methyl formamide	Alfa Aesar	CAS: 123-39-7
Poly(ethylene oxide)	Polysciences Inc.	CAS: 25322-68-3
Propylene oxide	Acros Organics	CAS: 75-56-9
Acetone	Sigma-Aldrich	CAS: 67-64-1
Acetonitrile	Sigma-Aldrich	CAS: 75-05-8
Methanol	Sigma-Aldrich	CAS: 67-56-1
Hexanes, mixture of isomers	Sigma-Aldrich	CAS: 107-83-5
Pentane	Sigma-Aldrich	CAS: 109-66-0
Software and algorithms		
Chemstation C.01.08	Agilent	https://www.agielnt.com/
OriginPro 2015	OriginLab	https://www.originlab.com/
Mnova14	Mestrelab	https://www.mestrelab.com/
Other		
Quaternary Pump	Agilent	Agilent Infinity II – G711B
Autosampler	Agilent	Agilent Infinity II – G7129A
Mass Spectrometry Detector	Agilent	Agilent Infinity Labs – G6125B
400 MHz Nuclear Magnetic Resonance Spectrometer	Bruker	AVANCE III HD 400
Fourier Transform Infrared Spectrometer	Bruker	Tensor 27
X-ray Diffractometer	Bruker	D8 ADVANCE
Thermogravimetric Analysis	NETZSCH	STA 4493
Scanning Electron Microscope	Thermo Fisher	Quattro
pH Meter	Fisher Scientific	Accumet AE150

RESOURCE AVAILABILITY

Lead contact

Further information and requests for resources and reagents should be directed to and will be fulfilled by the corresponding author, Jesús M. Velázquez (jevelazquez@ucdavis.edu).

Materials availability

The study did not generate any unique reagents.

Data and code availability

● All the data reported in this paper will be shared by the lead contact upon request.

- This paper does not report original code.

- Any additional information required to reanalyze the data reported in this paper is available from the lead contact upon request.

METHOD DETAILS

Chemicals and materials

Hafnium(IV) tetrachloride (98%) was used as the Hafnium source. Acetone, acetonitrile, hexanes, methanol, and pentane were all HPLC Plus (>99.9%). Hydrochloric acid (35.0–37.0%), sulfuric acid (95.0–98.0%), Sodium chloride (>99%) and deuterated water (D_2O) were used as purchased from Sigma-Aldrich. *N*-Methyl formamide (99%) and sodium hydroxide pellets (98%) were purchased from Alfa Aesar. Poly(ethylene oxide) (MW 100 000) was purchased from Polysciences Inc. Propylene oxide (99.5%) and Trifluoroacetic acid (99.5%) were purchased from Acros Organics. Perfluorooctanoic acid (>98%) was purchased from TCI America. Ultrapure water (≥ 18.2 M$\Omega \cdot$cm) used for synthesis and adsorption kinetics experiments was obtained from a Thermo Scientific Barnstead E-Pure Ultrapure water purification system.

MHO synthesis

MHO ceramic was synthesized using the sol–gel method detailed in our previous work (Hussain et al., 2020). Briefly, 20 mL scintillation glass vials were treated in sequence with 0.1 M NaOH for 1 hour, 0.1 M HCl for 1 hour, and Rain-X overnight prior to the start of the synthesis. After removing the Rain-X, vials were rinsed with methanol three times and dried in an oven at 150°C for 1 hour. Hafnium (IV) chloride was first hydrolyzed in ultrapure water. *N*-methylformamide was added as a porogen, to increase the solution pH and induce phase separation. Polyethylene oxide was added to create a strong pore network. Additionally, propylene oxide was added to polymerize the clear liquid into a white gel. The gel was then aged at 50°C for three days. The monolith was successively washed with ultrapure water, methanol, acetone, hexanes, then pentane to remove any excess reagents. Lastly, the sample underwent heat treatment in air to 700°C to yield a crystalline white monolithic ceramic. The concentration of reagents, gel aging time and drying time were kept consistent during each synthesis to maintain mesopore size (Brinker et al., 1994).

MHO characterization

The distinctive mesostructured morphology of the as-synthesized MHO ceramic was confirmed by a Thermofisher Quattro ESEM. To avoid charge mitigation from insulating surfaces such as MHO, samples were placed on double sided copper tape and operated at an accelerating voltage of 10 keV under low vacuum. The phase purity and crystalline structure of the adsorbent was determined by powder XRD using a Bruker D8 Advance diffractometer with Cu Kα radiation (1.5406 Å). Experimentally obtained diffraction patterns were then compared to literature patterns from the Inorganic Crystal Structure Database (ICSD) to confirm the structure. Thermogravimetric Analysis (TGA) was done on MHO powders before and after PFOA adsorption using a NETZSCH STA 449F3 instrument under high purity argon. It was heated from 20°C to 750°C at a rate of 10.0°C/min. The surface of the MHO ceramic was analyzed before adsorption, after adsorption, and after heating to remove PFOA (500°C) using Fourier transform infrared (FTIR) spectroscopy. The Bruker Tensor 27 FTIR was equipped with an attenuated total reflectance (ATR) pike accessory. The experiment was performed using 32 scans, a resolution of 2 cm^{-1}, and a spectral range of 400–4,000 cm^{-1}. The surface area was measured by Brunauer-Emmet-Teller (BET) method with nitrogen adsorption, and the Barrett-Joyner-Halenda (BJH) method was applied to determine average pore size using a Micromeritics Gemini VII surface area analyzer. The point of zero charge (pH_{PZC}) of MHO was analyzed using the pH drift method (Xie et al., 2016). The pH_{PZC} (point of zero charge) is the pH when the charge on the surface is neutral. The first step is to prepare a 0.01M NaCl solution using ultrapure water. Six Falcon tubes were filled with 50 mL of 0.01M NaCl. Then, the pH values were adjusted using 0.1M NaOH and 0.1M H_2SO_4 to be pH 2,4,6,8,10, and 12. Once the pH of solutions had stabilized the pH were recorded as $pH_{initial}$. Then 150 mg of crushed MHO was added to each Falcon tube and placed on the benchtop shaker for 24 hours to reach equilibrium. pH after shaking was recorded as pH_{final}. The pH_{PZC} of MHO is the point when $pH_{initial} = pH_{final}$.

PFOA adsorption kinetics, isotherm models, and desorption

PFOA adsorption experiments were performed using a Benchmark tabletop shaker. The white ceramic MHO was crushed and sieved to be between 0.6 and 2 mm. Each 50 mL Falcon tube contained 1.25 g of

MHO ceramic and 50 mL of PFOA solution in the range of 200–1,000 ppm. The concentration of PFOA used in the experiments was higher than the concentrations found typically in wastewater streams for ease of sample handling and analysis. Adsorption experiments were also performed using an initial concentration of 1 ppm PFOA at which micelles will not form in solution (Yu et al., 2009). Using a lower concentration will allow a better understanding of the adsorption behavior of PFOA on MHO at environmentally relevant concentrations. The pH was adjusted in these experiments using 0.1M NaOH and 0.1M H_2SO_4. The tubes were shaken for 12 hours, and a 1 mL aliquot was extracted every 2 hours for analysis. At the end of the 12 hours, the solid MHO floated on top and was separated from the liquid by filtration. The quantity of PFOA adsorbed per gram of MHO at a time t (q_t) was calculated using the following equation:

$$q_t = \frac{(C_0 - C_t) \times V}{m}$$ (Equation 1)

where C_t is the concentration at a time t, C_0 is the initial PFOA concentration, m is the mass of MHO, and V is the total volume of solution used in the adsorption experiment. To determine the order of the adsorption of PFOA on MHO, the data was fit to the pseudo-first-order (Equation 2) and pseudo-second-order (Equation 3) kinetic equations as depicted below:

$$\ln(q_e - q_t) = \ln q_e - k_1 t$$ (Equation 2)

$$\frac{t}{q_t} = \frac{1}{k_2 q_e^2} + \frac{t}{q_e}$$ (Equation 3)

where q_e is the adsorption capacity at equilibrium and q_t is the adsorption capacity at a time t and k_1 and k_2 are the rate constants for the pseudo-first-order and pseudo-second-order kinetic equations respectively. Langmuir (Equation 4) and Freundlich (Equation 5) adsorption isotherms were applied to further comprehend the adsorption of PFOA on MHO.

$$q_e = q_m K_L \frac{C_e}{1 + K_L C_e}$$ (Equation 4)

$$q_e = K_F C_e^{1/n}$$ (Equation 5)

where q_e is the adsorption capacity of PFOA on MHO at equilibrium, q_m is the saturation adsorption capacity, C_e is the concentration of PFOA at equilibrium, n is a constant relating to surface heterogeneity, and K_L and K_F are the Langmuir and Freundlich constants, respectively.

For the desorption experiment, the liquid was decanted after 12 hours of adsorption and 50 mL of ultrapure water adjusted to pH 2.3 was added to the spent MHO solid. After 12 hours of shaking, a liquid aliquot was collected and PFOA concentration was analyzed using ^{19}F NMR spectroscopy. All experiments were performed in triplicates and the average values are reported.

MHO reusability for PFOA adsorption

Spent MHO is regenerated after adsorption by heating at 500°C for twenty minutes. To determine the reusability of MHO for PFOA adsorption, the regenerated MHO was used for adsorption of PFOA. The adsorption experiments were performed using a Benchmark tabletop shaker. Each Falcon tube contained 1.25 g of MHO ceramic and 50 mL of 1,000 ppm PFOA at pH 2.3. The tubes were shaken for 12 hours, and a 1 mL aliquot was extracted every 2 hours for analysis. At the end of the 12 hours, the solid MHO floated on top and was separated from the liquid by filtration. The quantity of PFOA adsorbed per gram of MHO at a time t (q_t) was calculated (using Equation 1). Two more regeneration-adsorption cycles were performed on the spent MHO by heating at 500°C for twenty minutes after each adsorption experiment for a total of three regeneration cycles. The experiments were performed in triplicates and the average values are reported.

PFOA liquid analysis

The PFOA concentration in the liquid was quantitatively determined using ^{19}F nuclear magnetic resonance (NMR) spectroscopy on a Bruker 400 MHz spectrometer. The concentration was determined by integrating the area of the characteristic peak of the terminal CF_3 (−80.8 ppm) and comparing it to the area of the peak of the internal standard, trifluoroacetic acid (−76 ppm). Calibrations were performed with six standard solutions in the range of (9–2,000 ppm). 200 μL of liquid was added to 400 μL of D_2O spiked with TFA in a 300 MHz Wilmad NMR tube. The calibration curve is included in Figure S13, illustrating an R^2 value of

0.999. The limit of detection was found to be 18 ppm and the limit of quantification was found to be 100 ppm.

For liquid samples at a concentration of 1 ppm or lower, Liquid Chromatography Mass Spectrometry (LC-MS) was used to determine concentration. A five-point calibration curve ranging from 31.25 ppb to 500 ppb was constructed by diluting a 1 ppm PFOA standard in ultrapure water. Individual samples were diluted fivefold with ultrapure water prior to analysis. PFOA was analyzed by liquid chromatography (Agilent Infinity II quaternary pump - G711B) coupled to a single quadrupole mass spectrometer (Agilent - G6125B). 5 μL of each standard and sample were injected into a 2.1 × 100 mm C18 column (Agilent SB-C18 Poroshell 120 with 1.9 um pore size). PFOA was eluted at 0.200 mL/min using a gradient from 75:25 water/ acetonitrile (ACN) to 0:100 water/ACN over 5 minutes, 1 minute hold at 100% ACN, 100% ACN to 75:25 water/ACN over 1 minute, followed by 8 minutes at 75:25 water/ACN to re-equilibrate the column. Mass spectra were acquired via single ion monitoring (SIM) on 369 m/z and 413 m/z corresponding to the $[M - CO_2 - H]^-$ and $[M - H]^-$ ions, respectively. Mass spectrometry detection parameters were as follows: capillary voltage: -3500 V; drying gas flow rate: 12 L/min; drying gas temperature: $350°C$ nebulizer pressure: 35 psi; and fragmentor set to 70. The linear regression and sample concentration were calculated using the area under the curve.